

Physics of lithium bromide (LiBr) solution dewatering through vapor venting membranes



Rasool Nasr Isfahani, Abdy Fazeli, Sajjad Bigham, Saeed Moghaddam *

Department of Mechanical and Aerospace Engineering, University of Florida, Gainesville, FL 32611, United States

ARTICLE INFO

Article history:

Received 9 May 2013

Received in revised form 11 August 2013

Accepted 21 August 2013

Available online 31 August 2013

Keywords:

Absorption refrigeration systems

Lithium bromide

Desorption

Membrane-based desorber

Vapor venting membranes

Two-phase flow

ABSTRACT

The physics of water desorption from a lithium bromide (LiBr) solution flow through an array of microchannels capped by a porous membrane is studied. The membrane allows the vapor to exit the flow and retains the liquid. Effects of different parameters such as wall temperature, solution and vapor pressures, and solution mass flux on the desorption rate were studied. Two different mechanisms of desorption are analyzed. These mechanisms consisted of: (1) direct diffusion of water molecules out of the solution and their subsequent flow through the membrane and (2) formation of water vapor bubbles within the solution and their venting through the membrane. Direct diffusion was the dominant desorption mode at low surface temperatures and its magnitude was directly related to the vapor pressure, the solution concentration, and the heated wall temperature. Desorption at the boiling regime was predominantly controlled by the solution flow pressure and mass flux. Microscale visualization studies suggested that at a critical mass flux, some bubbles are carried out of the desorber through the solution microchannels rather than being vented through the membrane. Overall, an order of magnitude higher desorption rate compared to a previous study on a membrane-based desorber was achieved.

Published by Elsevier Ltd.

1. Introduction

Vapor compression systems (VCSs) could be considered as one of the technologies that have helped shape modern civilization. VCSs have greatly enhanced our standard of living and enabled the development of large population centers, even in very harsh climates. Increased access to electricity in the later part of the 19th century and better performance and operational characteristics of VCSs triggered the gradual replacement of the cooling system of the time (i.e. absorption refrigeration systems, ARSs) with VCSs. Despite their great benefits, VCSs consume significant electrical energy and use refrigerants that are not environment friendly. According to the US DOE (2012), buildings consume 72% of the nation's electricity, a great fraction of which is utilized for space cooling/heating, dehumidification, and hot water heating. The use of these amenities is rapidly rising in developing countries. In addition, refrigerant emission from VCSs in developing countries is expected to increase by as much as 800% more than emissions rate from VCSs in developed counties by 2050 (Velders et al., 2009). Thus, development of alternative, more efficient technologies can greatly enhance the future prospect of the world energy, environmental sustainability, and human quality of life.

ARSs have the potential to play a larger role in our future energy economy, since they can utilize low-grade thermal energy (e.g. waste heat and solar-thermal energy) for cooling and heating, if high performance, inexpensive, and robust systems are developed. To build compact and inexpensive systems, alternative heat exchanger configurations and system architectures have been studied (Islam et al., 2003; Yoon et al., 2006; Determan and Garimella, 2011; Garimella et al., 2011; Yu et al., 2012; Nasr Isfahani and Moghaddam, 2013; Ali and Schwerdt, 2009; Ali, 2010; Kang et al., 2000; Herbine and Perez-Blanco, 1995; Palacios et al., 2009; Yoon et al., 2005). Such systems are particularly attractive in solar-thermal energy harvesting and in combined heating, cooling and power (CCHP) systems where in the ARS is powered by the waste heat.

Depending on the choice of working fluid pairs, absorption systems are classified into ammonia–water and lithium bromide–water (LiBr–water) systems. In a LiBr–water system, water is used as the refrigerant and LiBr solution as the absorbent. The size of heat exchangers involved in absorption and desorption of water is impacted by the limited water mass transfer coefficient in the LiBr solution. Enhancement of the absorption and desorption transport processes and introduction of compact heat exchanger architectures facilitate development of economical small-scale systems.

Desorbers involving nucleate pool boiling (Charters et al., 1982; Lee et al., 1991; Varma et al., 1994) and falling film over horizontal or vertical tubes (Matsuda et al., 1990a, 1990b; Kim and Kim,

* Corresponding author. Tel.: +1 352 392 0889.

E-mail address: saeedmog@ufl.edu (S. Moghaddam).

1999) are the common configurations studied in the literature. In the pool boiling configuration, as the name implies, water is boiled off from a pool of LiBr solution. In a falling film desorber, the LiBr solution is sprayed over a tube bundle while the heating medium flows inside the tubes. The falling-film type desorbers are more suitable particularly with low temperature heat sources (Fujita, 1993) since formation of thin solution films over the tubes facilitates water desorption. At low surface temperatures, water directly diffuses out of the solution film as long as the solution temperature is high enough to sustain a solution water vapor pressure above the vapor pressure. Studies conducted by Charters et al. (1982) and Yoshitomi et al. (1981) suggest that a superheat temperature (the difference between the wall and the solution saturation temperatures) of approximately 10 °C is required for boiling inception.

The existing literature provides limited insight on the physics of LiBr solution boiling. The water ebullition process in a LiBr solution is fundamentally different from that which occurs in pure water. It is known that the water bubble growth rate is significantly slow (Nakoryakov et al., 1998) because of the low water diffusion coefficient in the LiBr solution. In other words, bubble growth in the LiBr solution is limited by mass diffusion rather than by heat transfer, as in pure water. Consequently, a significant surface superheat temperature is required to grow the bubbles large enough so that they can depart from the heat transfer surface (the buoyancy force should overcome the surface tension force for departure). Slow growing bubbles at moderate surface temperatures impede the surface heat transfer (Nakoryakov et al., 1998). Lee et al. (1991) investigated the pool boiling of LiBr solution at saturation conditions on a heated vertical tube. A higher desorption rate was achieved as compared to a horizontal tube configuration. Lee et al. (1991) argued that agitation of the LiBr solution near the surface is responsible for the higher performance. In addition, they reported a significant decrease in bubble size and an increase in surface heat flux (i.e. desorption rate) as the system pressure was increased.

Kim and Kim (1999) studied desorption from falling films on tubes tested at wall superheat temperatures of less than 10 °C to avoid boiling. They observed enhancement in desorption rate with an increase in desorber pressure and argued that high solution temperatures at elevated desorber pressures lower the solution viscosity and thickness over the tubes. A thinner solution film was considered responsible for the observed increase in the desorption rate. Shi et al. (2010) examined the heat transfer performance of a falling film desorber and reported a heat transfer coefficient more than four times higher, prior to boiling inception, than that of an immersed tube desorber.

In an attempt to reduce the solution film thickness and enhance the desorption rate, Thorud et al. (2006) mechanically constrained the LiBr solution flow between a solid wall and a heated porous membrane. The surface tension forces at the membrane–solution interface prevented the LiBr solution from seeping through the pores. Thorud et al. (2006) conducted studies on devices with 170 μm and 745 μm thick solution channels and primarily at high superheat temperatures associated with the boiling regime. The desorption rate was higher at the 170-μm-thick solution channel and enhanced with an increase in pressure difference across the membrane. However, the overall desorption rate was significantly less than that of the falling film desorbers. Thorud et al. (2006) do not discuss causes of the poor performance.

Thorud et al.'s (2006) work seems to be the sole published effort on the use of porous membranes for dewatering of the LiBr solution. However, studies on implementation of membranes for venting bubbles from a two-phase water stream exist (Meng et al., 2006; Johnson et al., 2009; Lochovsky et al., 2012; Kamitani et al., 2009; Zhu, 2009; David et al., 2009, 2011; Xu et al., 2010) that can provide some insights on characteristics of the process.

Meng et al. (2006) showed that hydrophobic membranes could be utilized to successfully vent bubbles from a water stream. Zhu (2009) demonstrated that the separation rate of the bubbles is directly proportional to the pressure difference applied across the membrane. Xu et al. (2010) suggested a set of criteria that must be met for a bubble to be entirely removed from a two-phase stream capped by a hydrophobic membrane. They argued that the bubbles should stay in contact with the membrane at a velocity lower than a critical value. Otherwise, a stable liquid layer forms between the bubble and the membrane and prevents bubble extraction.

This study is aimed at understanding the physics of the desorption process involved in a thin LiBr solution flow mechanically constrained by a nanofibrous polytetrafluoroethylene (PTFE) membrane. An experimental LiBr–water ARS is built to test a membrane-based desorber at the working conditions of a typical ARS desorber. The experiments are conducted in both single- and two-phase modes (cf. Fig. 1) to identify the parameters affecting the processes and to quantify their impact. A numerical model developed in a prior study (Yu et al., 2012) is used to analyze the single-phase desorption process. To better understand the results of the two-phase desorption mode, a micro-scale visualization study is conducted in a separate test platform.

2. Experimental setups

2.1. Membrane-based desorber heat exchanger

A schematic of the desorber heat exchanger cross-section is provided in Fig. 2. The desorber consists of: (1) a corrosion-resistant C-22 Hastelloy plate in which the solution microchannels are machined (2) a brass enclosure with a sight glass (cf. Fig. 3a). The overall size of the desorber is 16.8 × 16.5 cm². The solution microchannels are machined over a 5.7 × 8.9 cm² area. A nanofibrous PTFE membrane with a pore size of 0.45 μm and a thickness of 50 μm is placed on the solution microchannels and secured in place by a perforated stainless steel sheet. Twelve thermocouples are installed within three trenches machined on the backside of the Hastelloy plate to measure the wall temperature. The remaining space within the trenches is filled with a high temperature thermally conductive epoxy and a flexible thin-film heater (Omega Engineering, CT) is subsequently assembled over the entire surface. Fig. 3a shows a photograph of the assembled desorber heat

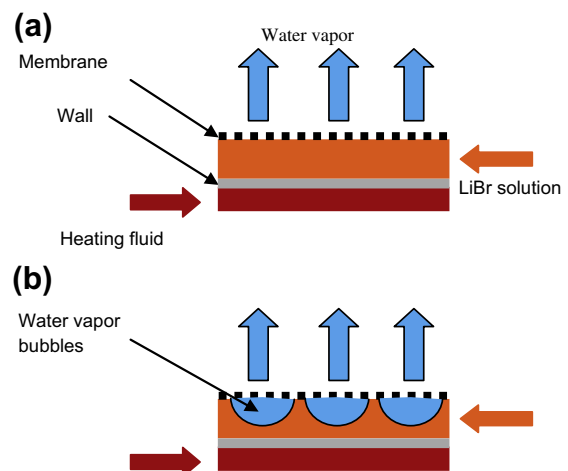


Fig. 1. Schematic representation of membrane-based desorption process showing (a) direct diffusion of water from the solution flow and (b) bubble formation and desorption through the membrane during the boiling regime.

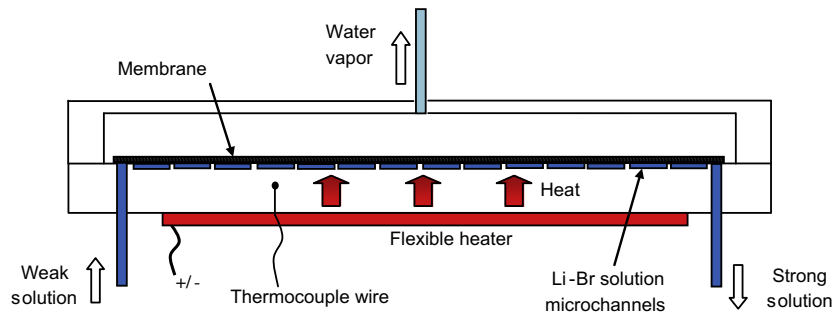


Fig. 2. Schematic diagram of the desorber heat exchanger.

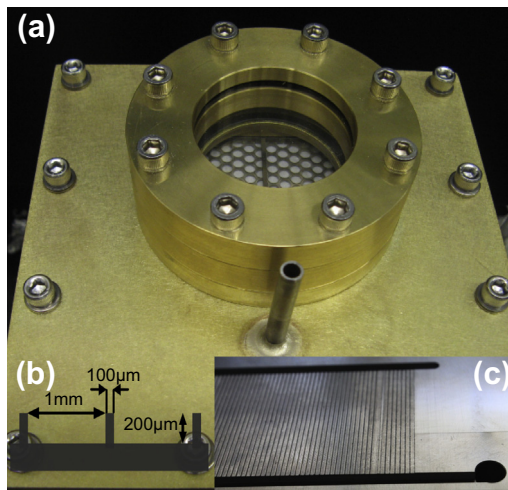


Fig. 3. (a) A photograph of the assembled desorber heat exchanger, (b) a dimensioned schematic of the solution microchannels and (c) a photograph of the solution microchannels.

exchanger. Fig. 3b and c show a schematic of the cross section and a photograph of the microchannels, respectively.

2.2. Desorber test system

Fig. 4 shows a diagram of the experimental loop in which the membrane-based desorber was tested. The loop consists of a LiBr solution line and a refrigerant (water) line. The solution line consists of an absorber, a desorber, a pump, a filter, a solution reservoir, a Coriolis mass flow meter, and two solution heat exchangers. The water line consists of an evaporator, a condenser, a Coriolis mass flow meter, and a water reservoir. In the solution line, a micro gear pump (HNP Mikrosysteme, Germany) drives the weak LiBr solution through a solution heat exchanger, where the solution is preheated to a desired temperature before entering the desorber. In the desorber, the weak LiBr solution is heated by a thin film heater (Omega Engineering, CT) to desorb water. The desorbed water vapor flows to a condenser, and the strong LiBr solution leaves the desorber and flows through a heat exchanger, where it is cooled to a preset temperature before entering a Coriolis mass flow meter (Bronkhorst USA) and then the absorber. The condensed water leaves the condenser and flows through a Coriolis mass flow meter (Micro Motion, CO) to the evaporator, where it is vaporized and supplied back to the absorber. The strong solution flows through the absorber and absorbs the water vapor generated in the evaporator. The weak solution leaving the absorber flows through a filter and is pumped back to the solution pre-heater and then to the desorber to complete the cycle.

The solution heat exchangers (i.e. HX1 and HX2, depicted in Fig. 4) that control the inlet temperature to the absorber and desorber are cooled or heated using thermoelectric cooling/heating (TEC) units. The heat exchangers are made of Inconel coil, fabricated through forming tubes, which are assembled within two aluminum plates with machined grooves to accommodate the coil. The TECs are attached to the heat exchanger assembly (i.e. on the aluminum surface) using a thermally conductive adhesive sheet. The TECs have air-cooled heat sinks and fans. The outlet temperature of each solution heat exchanger is controlled using its corresponding TEC control panel. A similar tube heat exchanger with a temperature controller is used for the condenser. The desorber and evaporator heat exchangers are heated using flexible heaters. The applied power to the heaters is controlled manually. DC power supplies are used to provide power to the heaters and the TECs.

The experimental setup is also equipped with two small reservoirs with sight glass to monitor the liquid in the solution and water lines. These reservoirs also serve as compensation chambers and assist in proper charging of the system. Inconel tubing and Monel fittings that are highly corrosion resistant are used in the assembly of the solution line, and stainless steel tubing and fittings are used in the water line.

Thermocouple probes (Omega Engineering, CT) with Inconel sheath are used to measure the solution temperature at the inlet and outlet of the absorber and desorber. The vapor temperature in the condenser and evaporator is measured by probes with stainless steel sheath. The solution and water mass flow rates and densities are measured using two Coriolis mass flow meters. Three pressure transducers with a range of 0–100 kPa are installed to monitor desorber pressure conditions. Two of the transducers measure the LiBr solution flow pressure at the desorber inlet and outlet. The average solution pressure (P_s) is calculated using the readings of these transducers. The third transducer measures the vapor pressure (P_v) at the desorber vapor exit (the outlet tube seen in Fig. 3a). All the measured data are recorded by a data acquisition system.

2.3. Visualization test section

Fig. 5 shows a schematic of the device used for microscale visualization studies of bubbles extraction process through the nanofibrous membrane utilized in the desorber. The device consists of a polydimethylsiloxane (PDMS) chip on which flow channels are built. PDMS is transparent and enables visualization of the bubbles during the venting process through the membrane. Water and air are injected into the device at various flow rates through a T-junction to create a two-phase flow with a controlled quality. The water and air supply channels are 500- and 100- μm -wide, respectively. The main flow channel, where the bubble extraction process takes place, is 1000- μm -wide and 200- μm -deep. The PDMS device is fabricated through a standard soft-lithography technique (Qin

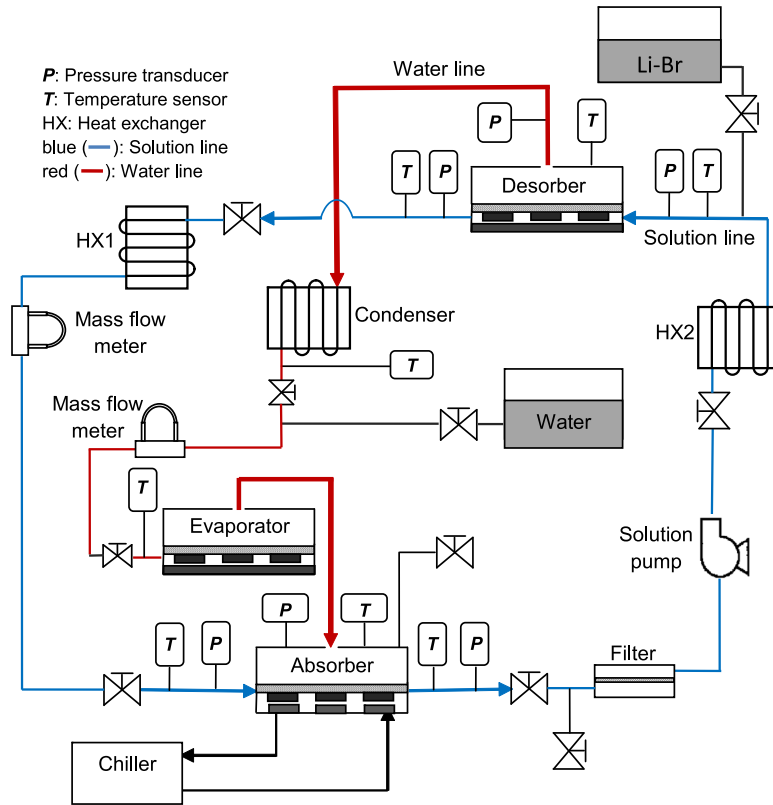


Fig. 4. Schematic diagram of the experimental setup.

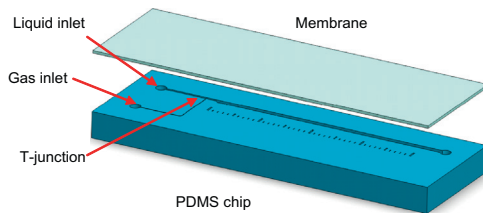


Fig. 5. A 3D schematic of the visualization test device.

et al., 2010). The PTFE membrane was subsequently bonded on the device, as shown in Fig. 5.

2.4. Visualization test system

Fig. 6 shows a diagram of the visualization test system. Two syringe pumps (Fisher Scientific Inc., PA) are used to deliver water and air to the test device. PX-26 transducers (Omega Engineering, CT) with a range of 0–5 psi are used for pressure measurements. Images of the bubbles during the extraction process are captured using a high speed Gazelle camera (Point Grey Research Inc., Canada, BC).

2.5. Experimental procedure

The experimental ARS was charged with a 55% LiBr solution inhibited by Lithium Molybdate (Leverton-Clarke Ltd., UK). The water line was charged with degassed and deionized water. Each experimental run began by operating the solution pump and setting the flow rate at a desired value. The water chiller was then turned on and the temperature of the absorber cooling water was set. A valve between the evaporator and the absorber was then

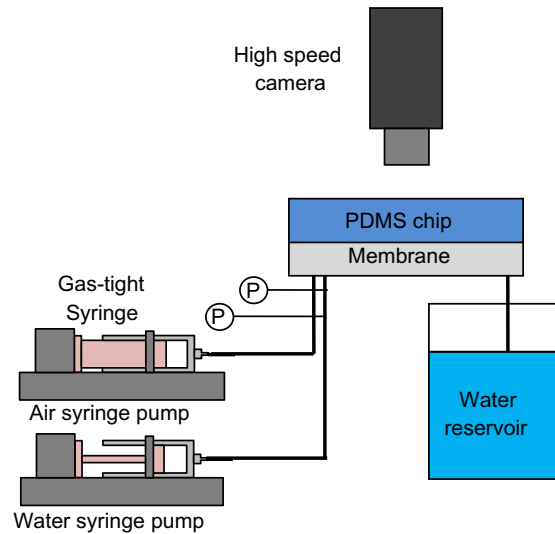


Fig. 6. A diagram of the visualization test system.

opened and the absorption process began. Next, the TEC modules were turned on and the inlet temperatures to the absorber and desorber heat exchangers were set. Once the desired temperatures were reached, the desorber and evaporator heaters were powered on. Changes in temperatures, pressures, and mass flow rates were monitored continuously. The system was assumed to have reached steady-state when variations in the desorber vapor pressure, solution density, and wall temperature were within 10 Pa, 5 kg/m³, and 1 °C, respectively, for at least 30 min. The desorption rate was then directly measured by the mass flow meter on the water line. Studies were conducted on the effects of wall temperature, vapor

Table 1
Input values for membrane-based desorber parametric studies.

Parameter	Nominal	Range
LiBr–water solution flow rate (\dot{m}_{sol})	2.5 kg/h	0.75–3.25 kg/h
LiBr–water solution pressure (P_s)	23 kPa	13–30 kPa
LiBr–water solution temperature at desorber inlet (T_{in})	70 °C	NA
Vapor pressure (P_v)	10 kPa	6–18 kPa
Average wall temperature (T_w)	NA	50–125 °C

pressure, solution pressure, and solution velocity on the desorption rate. Table 1 summarizes the tests' conditions. Note that pressure in a typical desorber heat exchanger of a single effect ARS is approximately 10 kPa. Efforts were made to maintain the solution concentration (i.e. the LiBr weight fraction) in the desorber close to that of an actual system. The solution flow rate and the heater power were adjusted to achieve this objective. These parameters were carefully controlled to avoid crystallization of the solution that occurs if the solution concentration at the desorber exit exceeds the LiBr solubility limit (cf. Fig. 7).

In the visualization tests, bubbles images were recorded at least 500 s after the flow reached a steady state.

2.6. Experimental uncertainty

Table 2 lists uncertainty in measurement of pressure, concentration, solution flow rate, and temperature. The accuracy of the water mass flow meter that directly measures the water desorption rate at the condenser exit is $\pm 1\%$. However, due to the unsteady nature of the condensate flow, a fluctuation of up to $\pm 5\%$ was recorded during the experiment. The reported desorption rates are the average of the measured values over a period of time, after the system reached a steady state. The concentration uncertainty is calculated using the following equation.

$$\Delta X = \sqrt{\left(\frac{\partial X}{\partial \rho} \Delta \rho\right)^2 + \left(\frac{\partial X}{\partial T} \Delta T\right)^2} \quad (1)$$

where X and T are the solution concentration and temperature, respectively, and ρ is the solution density.

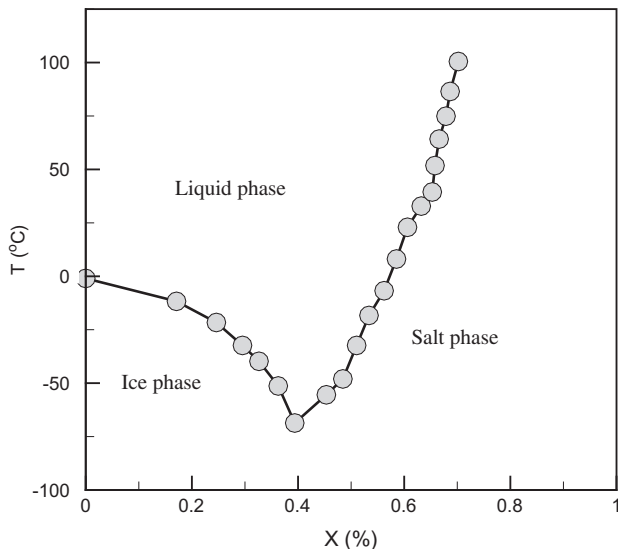


Fig. 7. Aqueous lithium bromide phase diagram (data determined from Herold et al. (1996)).

Table 2
Variable uncertainties.

Variable	Uncertainty
Pressure	0.5%
Concentration	± 0.25
Solution flow rate	0.2%
Temperature (°C)	0.3 °C

The uncertainty in the visualization tests results from ± 1 ml/h inaccuracy in pumping rate of the syringe pump and $\pm 1\%$ inaccuracy of the pressure transducers.

3. Data reduction

The solution mass flow rate and density are measured by the Coriolis mass flow meter installed in the solution line. The desorption rate is measured by the mass flow meter on the water line. The solution concentration is calculated using the measured density and temperature of the solution. The solution inlet concentration is then calculated using a mass balance on the desorber.

$$X_{in} = \frac{\dot{m}_{sol}}{\dot{m}_{sol} + \dot{m}_{des}} X_{out} \quad (2)$$

where X_{in} and X_{out} are the LiBr solution concentrations at the desorber inlet and outlet, respectively, \dot{m}_{sol} is the solution mass flow rate measured at the desorber outlet, and \dot{m}_{des} is the desorption rate.

The heat input to the desorber is calculated using

$$\dot{Q}_{des} = VI \quad (3)$$

where V and I are the applied voltage and current to the heater, respectively. This heat input is the sum of heat loss, sensible heat and latent heat of vaporization. The energy balance in the desorber can be written as:

$$\dot{Q}_{des} = \dot{m}_v h_v + \dot{m}_{sol} h_{sol}^o - (\dot{m}_{sol} + \dot{m}_v) h_{sol}^i + \dot{Q}_{loss} \quad (4)$$

where h_v is the enthalpy of water vapor leaving the desorber, h_{sol}^i and h_{sol}^o are the solution enthalpies at the desorber inlet and outlet, respectively, \dot{m}_v is the vapor generation rate, and \dot{Q}_{loss} is the desorber heat loss. Using Eq. (4), \dot{m}_v can be calculated as follows

$$\dot{m}_v = (VI + \dot{m}_{sol}(h_{sol}^i - h_{sol}^o) - \dot{Q}_{loss}) / (h_v - h_{sol}^i) \quad (5)$$

Note that \dot{m}_v is different from the desorption rate measured by the water line flow meter. The \dot{m}_v and \dot{m}_{des} (vapor flux desorbed through the membrane) would have been the same, if no bubbles exited the desorber through the solution line. The uncertainty in \dot{m}_v calculation is 0.3% and it is due to uncertainty in temperature, solution flow rate, and voltage and current measurements.

4. Membrane transport mechanism

Membranes can separate species when subjected to a driving potential. The driving potential could be the gradient of

temperature, pressure, concentration, or the electrical potential. Overall, the rate of transport through a membrane can be expressed based on the gradient of the chemical potential:

$$J_i = -L_i \frac{d\mu_i}{dx} \quad (6)$$

where J_i is the permeate flux, L_i is the coefficient of proportionality of permeate i , x is position along the membrane thickness, and μ_i is the chemical potential defined in Eq. (7) for incompressible phases and in Eq. (8) for compressible gases (Wijmans and Baker, 1995):

$$\mu_i = \mu_i^0 + RT \ln(\gamma_i c_i) + v_i(P - P_i^0) \quad (7)$$

$$\mu_i = \mu_i^0 + RT \ln(\gamma_i c_i) + RT \ln \frac{P}{P_i^0} \quad (8)$$

where μ_i^0 is the chemical potential of component i at a reference pressure of P_i^0 , c_i is the molar concentration of component i , γ_i is the activity coefficient, P is pressure, v_i is the molar volume of component i , T is temperature, and R is the gas constant. Calculations of the permeate flux using Eq. (6) require further assumptions about variations of pressure and concentration (cf. Eqs. (7) and (8)). Among different transport models, solution-diffusion model (Lonsdale et al., 1965) is widely utilized for transport through membranes. This model assumes that the chemical potential only changes due to concentration variations across the membrane. Using this model, for the case in which the membrane confines a multi-component liquid and only allows permeation of species i , a simple expression for permeate flux as a function of partial pressures is determined (Wijmans and Baker, 1995):

$$J_i = P_i^G (P_{s,i} - P_{v,i}) \quad (9)$$

where P_i^G is the permeability coefficient, $P_{s,i}$ is the partial vapor pressure of component i in the liquid, and $P_{v,i}$ is the partial pressure of component i in the vapor side. This equation suggests that the driving potential is the difference in the partial pressure of the permeate between the two sides of the membrane (cf. Ali and Shwerdt, 2009 and Ali, 2010).

5. Results and discussion

In the first set of tests, the effects of heated wall temperature on the desorption process were studied. Fig. 8 shows the data sets and

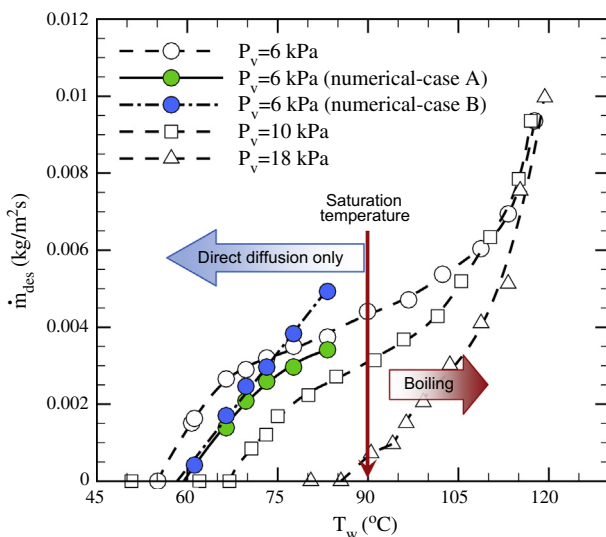


Fig. 8. Effect of heated wall temperature on desorption rate at different vapor pressures.

their corresponding interpolations. The wall temperature, T_w , is the average reading of the twelve thermocouples imbedded within the heated wall. The first test was conducted at 6 kPa vapor pressure. The other test parameters were kept constant at the nominal conditions listed in Table 1. The surface temperature was increased in approximately 5 °C increments until desorption started. The first non-zero desorption rate was measured at a surface temperature of approximately 60 °C. The desorption rate then steadily increased with surface temperature at a moderate pace until it started to significantly rise at a surface temperature of 95–100 °C, signifying a change to the desorption regime. This change was associated with some fluctuations in solution flow rate and pressure readings due to instabilities associated with boiling of the solution flow.

Using the thermodynamic properties of the LiBr solution and concentration at the desorber inlet, it was determined that the solution water vapor pressure ($P_{s,w}$) exceeded 6 kPa (i.e. the desorber vapor pressure) at a solution temperature of higher than 56 °C. The positive pressure (or chemical) potential (i.e. $P_{s,w} - P_v > 0$) across the membrane drove the desorption process with an onset of desorption at about 60 °C surface temperature (cf. Eq. (8)). The driving pressure potential, and consequently the desorption rate, further enhanced by increasing the surface temperature. Hereafter, this desorption mechanism is called “direct diffusion” mode of desorption, since water molecules directly diffuse out of the thin solution film and subsequently flow through the membrane. Desorption rate through this mechanism diminished when the vapor pressure was increased (cf. Fig. 8), due to decrease in pressure potential. The fact that the solution pressure (23 kPa) was always higher than the vapor pressure clearly suggests that desorption through this mechanism is not driven by the solution pressure. The solution pressure, as mentioned earlier, is the applied pressure on the liquid side of the membrane and is different from the solution water vapor pressure that is a thermodynamic property and a function of solution temperature and concentration. In essence, it is the difference between the solution water and vapor pressures that drives the water molecules through the solution film and the membrane.

As the results in Fig. 8 suggest, desorption through the direct diffusion mode increased linearly with temperature at low desorption rates. This is consistent with the theory because as the solution water pressure increases with temperature, the pressure potential driving the process increases. However, the rate of increase significantly declined at higher desorption rates. To understand the cause of this behavior, a numerical model of the desorber was prepared. The numerical model simulates the desorber geometry explained in Section 2.1 and uses the nominal experimental values listed in Table 1 as the model input, except that $P_v = 6$ kPa. Briefly, the model is a 89-mm-long and 200- μ m-deep channel capped by a membrane with 0.45 μ m pore size and a thickness of 50 μ m supported by a metal sheet with 3.2 mm openings that are space 2.1 mm apart. The numerical method used to solve the heat and mass transfer field is discussed in Yu et al. (2012). The numerical method is based on a continuum-based approach to model heat and mass transfer inside the solution and the Dusty-Gas model (Mason and Malinauskas, 1983) for simulation of the vapor flux through the membrane. The heat and mass transfer equations are solved using the Lattice Boltzmann Method (LBM).

A comparison of the numerical and experimental results is provided in Fig. 8. The most important observation is that the numerical simulation (case A in Fig. 8) closely captures the rate of change in the desorption rate and, as it will be discussed shortly, it was later used to successfully determine the factor responsible for the observed decline in the rate of increase in desorption rate. The absolute difference between the two results could be mostly due to the difference between the solution properties and the equation-of-state used for the LiBr-water solution (note that the

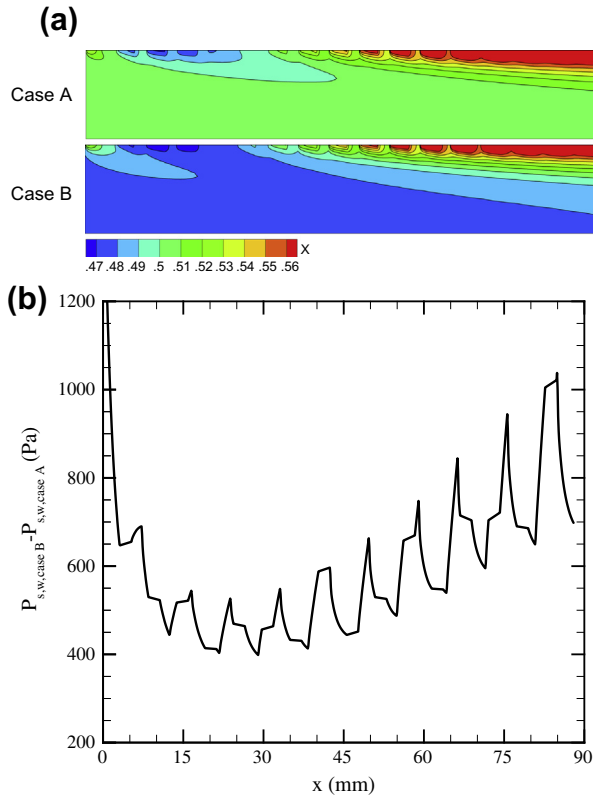


Fig. 9. Comparison of numerical results showing a lower concentration solution (or a higher solution water vapor pressure) in case B compared to case A. A scale factor of 0.013 is used in the x-direction to show the concentration contours over the entire flow domain (a). Water pressures used in (b) are determined at a distance of 20 μm below the vapor–liquid interface.

solution used in the system contains additives that could impact its properties) as well as the surface temperature and the liquid film thickness. Using the numerical model, it was determined that small variations in the solution concentration entering the desorbent are responsible for the observed behavior. Although efforts were made during the tests to maintain this parameter constant at 50%, the system stabilized at a slightly different concentration in each test. This resulted in an overall variation in concentration of 3% (change from 48% to 51%). Fig. 8 also provides numerical results at a hypothetical constant solution inlet concentration of 48%. A comparison of numerical results between cases A and B (cf. Fig. 8) at a wall temperature of 83 $^{\circ}\text{C}$ and a concentration difference of 3% is provided in Fig. 9. The comparison shows that a more water-rich (i.e. less concentrated) solution in case B provides a higher solution water vapor pressure and consequently a higher desorption pressure potential compared to case A.

As mentioned earlier, increasing the temperature a few degrees above the solution saturation temperature (87–90 $^{\circ}\text{C}$) significantly enhanced the rate of increase in desorption (cf. Fig. 8), due to boiling inception. Desorption through the boiling mode superimposed itself on the direct diffusion desorption mode and gradually dominated as the surface superheat temperature (i.e. the difference between the surface temperature and the solution saturation temperature) was increased. This is evidenced by the fact that the effect of vapor pressure on the desorption rate gradually declined to the extent that at a high superheat temperature, there is hardly a difference between the desorption rates at different vapor pressures. This is due to the fact that formation of bubbles generates a significant vapor–solution interface area within the microchannels resulting in a shorter diffusion path for the water molecules. The bubbles then vent through the membrane. The

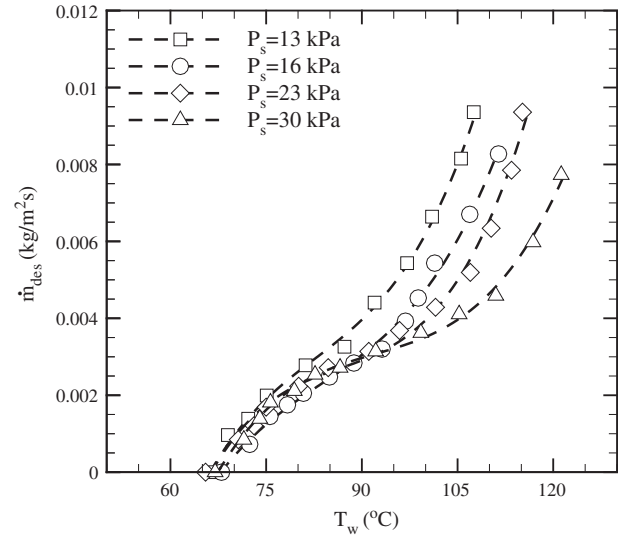


Fig. 10. Effect of solution pressure on desorption rate.

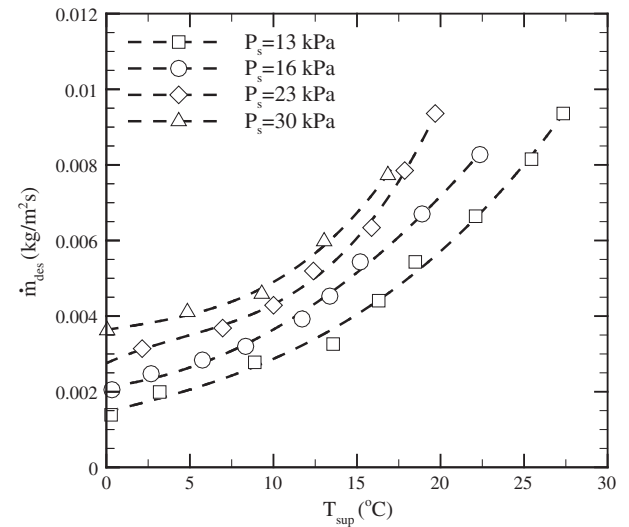


Fig. 11. Effect of solution pressure on the desorption rate in a boiling regime.

independence of bubbles venting rate from the pressure potential across the membrane suggests that the membrane mass transfer resistance is insignificant.

5.1. Effect of solution pressure

In the second set of tests, the solution pressure was changed from 13 kPa to 30 kPa while the other test parameters were kept constant at the nominal conditions. The results (cf. Fig. 10) reaffirmed that the effect of solution pressure on desorption through direct diffusion mechanism is insignificant. By contrast, changing the solution pressure significantly affects desorption through the boiling process. Increasing the solution pressure delays the transition to the boiling desorption mode. This is due to an increase in solution saturation temperature. It should be noted that the solution saturation temperature is a function of the solution pressure and concentration. Unlike a falling film desorbent, wherein the solution saturation temperature remains unchanged at a constant vapor pressure, in a membrane-based desorbent, the solution pressure can be controlled independent of the vapor pressure.

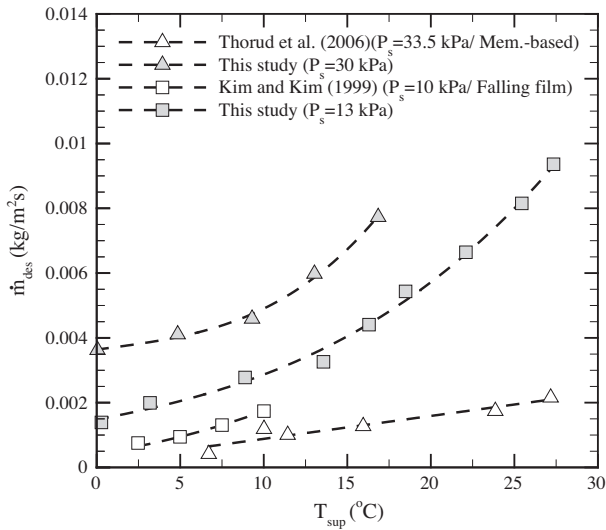


Fig. 12. Comparison of the measured desorption rate with those of other studies.

To filter out the effect of change in saturation temperature, the boiling desorption data were plotted versus the wall superheat temperature (cf. Fig. 11). The results suggest that increasing the solution pressure enhances the desorption rate through the boiling mode. An increase in pressure is known to enhance the heat transfer coefficient and heat flux in pool boiling (Nishikawa et al., 1982; Abuaf et al., 1985) and boiling in micro/minichannels (Rainey et al., 2003; Hu et al., 2011). Kocamustafaogullari and Ishii (1983) have shown that the boiling heat transfer coefficient is not only a function of the superheat temperature, but also a function of the active nucleation site density. An increase in pressure has been found to enhance the size range of activate cavities (Nishikawa et al., 1982; Hibiki and Ishii, 2003). Similar observations have been made in shell-and-tube desorbers. Lee et al. (1991) investigated the effect of solution pressure on pool boiling characteristics of a lithium bromide solution on a vertical tube. They observed that increasing the solution pressure and surface temperature significantly increases the number of active nucleation sites, reduces the bubble size, and enhances the desorption rate.

The results presented above are compared with those of Thorud et al. (2006) on a device with 170 μm thick solution channels (cf. Fig. 12). Thorud et al. (2006) reported a desorption rate an order of magnitude lower than that measured in this study. However, they did not discuss reasons for the lower desorption rate achieved even compared to falling film desorber results reported by Kim and Kim (1999), as shown in Fig. 12, which typically involves solution films thicker than 170 μm (Jani et al., 2004). Furthermore, it is not clear why their desorption rate versus superheat temperature graph does not exhibit characteristics associated with the boiling desorption mode (i.e. rapid increase in desorption rate with a small increase in surface superheat temperature). The device configuration and mass transfer resistance of the membrane used in their study could be responsible for the low performance. In their assembly, the solution film is heated on the same side that the generated vapor exits. It could be argued that since the vapor generated within the solution tends to accumulate at the membrane surface (because the membrane surface is hydrophobic), the thermal resistance between the heated surface and the solution increases when more vapor is generated. This could lead to a self-limiting process in which the heat supply to the solution, and hence the desorption rate, could only be enhanced by a proportional increase in temperature potential (i.e. the surface superheat temperature). Thorud et al. (2006) does not provide the

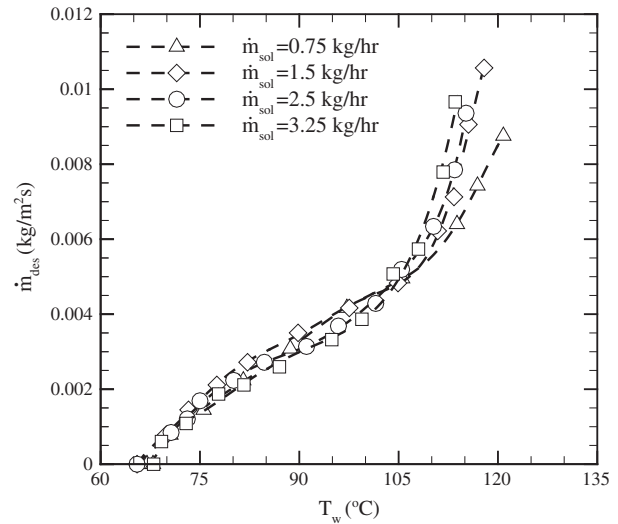


Fig. 13. Effect of solution flow rate on desorption rate.

membrane properties or a parametric study that identifies the membrane mass transport characteristics. Thus, it is not possible to attribute the membrane contribution to the poor performance.

5.2. Effect of solution velocity

To study the effect of flow velocity on the desorption rate, the solution flow rate was changed from 0.75 kg/h to 3.25 kg/h. The results (cf. Fig. 13) show almost no effect on the direct diffusion desorption mode, because desorption through this mode is limited by the rate of water molecules diffusion through the solution film, which remains unchanged as long as the flow regime is laminar. However, in the boiling mode, the desorption rate increased by as much as about 50%, since the supply of water-rich solution to the microchannels is enhanced. Since changes in the solution pressure and concentration result in change in saturation temperature, and consequently the desorption rate, the results can represent the effect of velocity alone only if the desorber's average concentration and solution pressure remain constant. The average solution pressure was kept constant at the nominal condition. At a given wall temperature, the average solution concentration varied by less than 1% at different solution flow rates. Therefore, the results presented in Fig. 13 represent the effect of solution velocity.

5.3. Analysis of bubbles discharge

As discussed earlier, in the boiling regime, bubbles form and subsequently exit the flow through the membrane. However, there is always a chance that some bubbles exit the desorber along with the solution flow (i.e. bubbles do not get extracted through the membrane). This is especially true for bubbles generated near the end of microchannels. This effect negatively impacts the efficacy of the desorber and the system. The fraction of bubbles exiting the solution flow can be determined using the desorber energy balance. To do so, the desorber heat loss to the ambient was measured as a function of desorber temperature. To measure the heat loss, all valves connected to the desorber were first closed and then the desorber heater was energized to hold the desorber at different temperatures. The energy supplied to the desorber to maintain it at any temperature is considered to be its heat loss. The results of this test are provided in Fig. 14.

Another fraction of the supplied heat to the desorber increases the solution temperature (i.e. turns into sensible heat). The

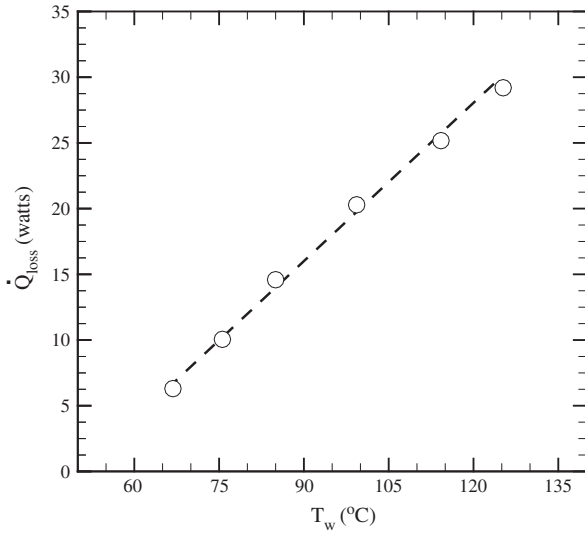


Fig. 14. Desorber heat loss as a function of its wall temperature.

sensible heat is calculated using the difference in enthalpies of the inlet and outlet solution flows. Fig. 15 compares the heat loss and sensible heat with the total heat supplied to the desorber at the nominal test conditions. The results suggested that the two terms account for a significant portion of the heat supplied to the desorber.

The heat consumed in water vapor generation is equal to the total heat supplied to the desorber minus the heat loss and the sensible heat. This balance is reflected in Eq. (4), which is used to calculate the vapor generation rate. Fig. 16 compares the generated vapor rate and the vapor flow rate through the membrane (measured by the water line flow meter) at different solution pressures (cf. Fig. 10). As can be seen in Figs. 16, the vapor generation rate closely matches the vapor flow through the membrane at the direct diffusion desorption mode. However, the difference between the two reaches a maximum of 15% in the boiling regime. This means that some of the generated bubbles were not extracted through the membrane (i.e. exited the desorber through the solution line). The results also suggest that the vapor flow through the

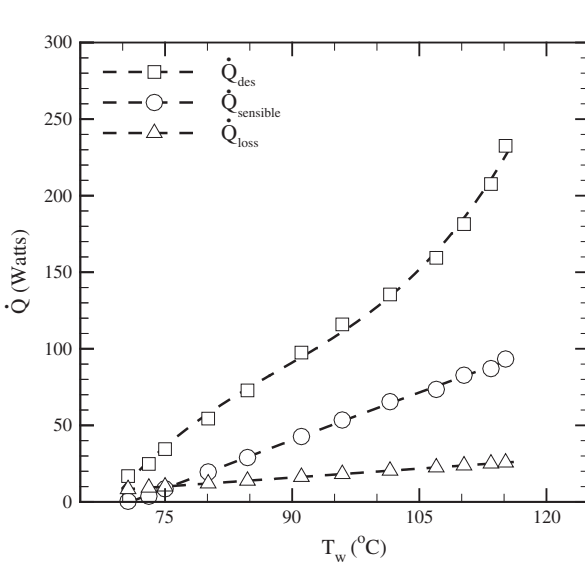


Fig. 15. Comparison of desorber heat loss and solution sensible heat to desorber input heat.

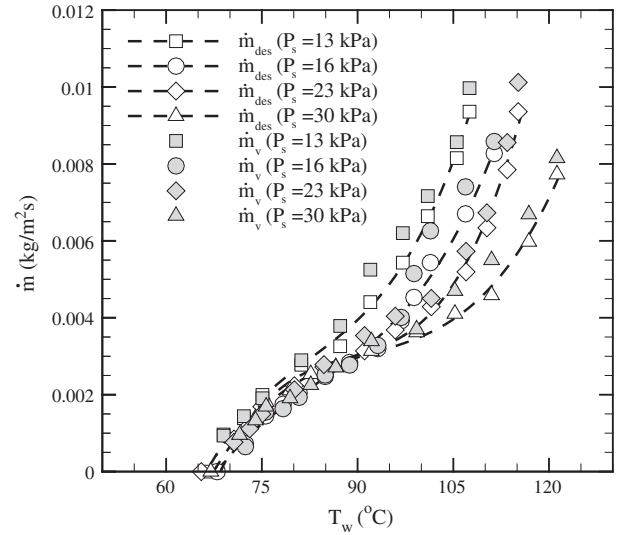


Fig. 16. Comparison of the vapor desorption and generation rates at different solution pressures.

solution line exit is not a function of the vapor flux through the membrane. This implies that the membrane mass transport resistance is not responsible for this phenomenon.

The vapor generation rate was also calculated for the results presented in Fig. 13, where the solution flow rate was changed. Fig. 17 provides the difference between the vapor generation and desorption rates (averaged for all tests) as a function of the solution flow rate. The corresponding solution mass flux (\dot{m}_{sol}'') was also calculated and is shown in the graph. The results suggest that increasing the solution flow rate enhances the vapor exit rate through the solution flow line. At a flow rate of 0.75 kg/h, the vapor generation and extraction rates were almost equal. Increasing the flow rate from 2.5 kg/h to 3.25 kg/h almost doubled the bubble escape rate through the solution line (from about 0.0005 kg/m² s to 0.0011 kg/m² s).

To understand the physics of bubbles escape through the solution line, further studies were conducted using the visualization test setup discussed earlier. The differential pressure across the

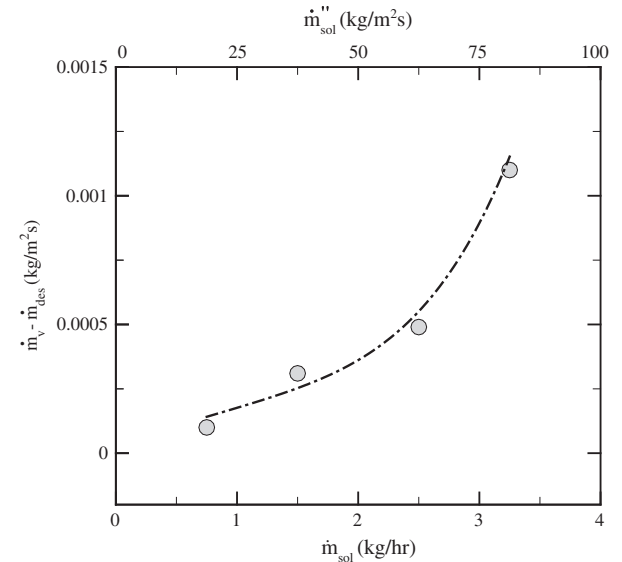


Fig. 17. Comparison of vapor desorption and generation rates at different solution flow rates.

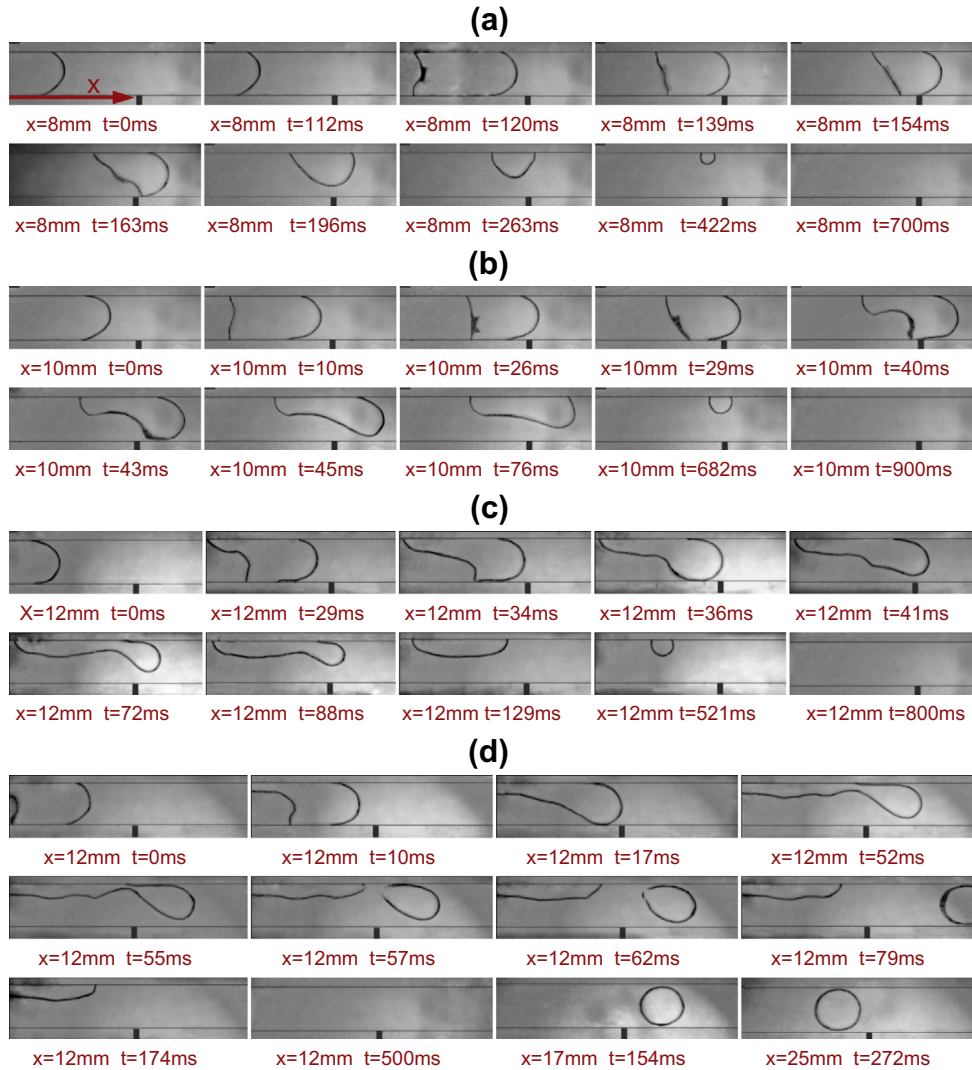


Fig. 18. Bubble extraction through the membrane with 13 kPa pressure difference across the membrane at three fluxes: (a) $\dot{m}_w'' = 12 \text{ kg/m}^2 \text{ s}$, (b) $\dot{m}_w'' = 41 \text{ kg/m}^2 \text{ s}$ (c-d) $\dot{m}_w'' = 54 \text{ kg/m}^2 \text{ s}$.

membrane was kept constant in all tests at 13 kPa to simulate the test conditions in Fig. 17. Tests were conducted at different mass flux. Fig. 18 shows the bubbles images during the venting process at different conditions. The x and t shown on the figures indicate distance from the device inlet and time. Fig. 18a shows test results at a water mass flux (\dot{m}_w'') of $12 \text{ kg/m}^2 \text{ s}$. At this condition, the bubbles fully vent through the membrane before moving much along the flow channel (about 8 mm). Increasing the flux to $41 \text{ kg/m}^2 \text{ s}$ only slightly delayed the bubble full extraction, as it is evident in Fig. 18b. However, signs of a transition to a different regime appeared in which increased drag force on the bubble significantly changed its shape. Further increase of the flux to $54 \text{ kg/m}^2 \text{ s}$ indicated that while some bubbles still completely vent through the membrane, albeit farther from the channel inlet (cf. Fig 18c), a portion of the bubble snaps off from the main bubble (cf. Fig 18d) and flows through the channel without venting through the membrane. This indicates that the bubble is no longer in contact with the membrane. Xu et al. (2010) showed that at a critical velocity, a liquid film forms between the bubble and the membrane and prevents bubbles extraction. The frequency of this event was approximately 30% at this flow rate. Increasing the flux to $83 \text{ kg/m}^2 \text{ s}$ enhanced the frequency of the event to 50%. Finally, at a flux of $110 \text{ kg/m}^2 \text{ s}$, almost all bubbles experienced the same phenomenon.

The overall physics and trends of the observed phenomena apply well for flow of vapor in a LiBr solution, with small variations due to differences in fluid properties. Of particular interest is the bubbles snapping events that occur when drag forces on a bubble exceed the surface tension forces. The surface tension of the LiBr solution at the boiling test conditions discussed earlier ranges from 0.0068 to 0.0076 N/m (Hasaba et al., 1961) that is quite close to that of water ($\sigma = 0.073 \text{ N/m}$) at room temperature. On the other hand, the shape drag force on a bubble is

$$F_D = \frac{1}{2} \rho V^2 C_d A = \frac{1}{2} \frac{\dot{m}''^2}{\rho} C_d A \quad (10)$$

where ρ is liquid density, V is the flow velocity, C_d is the drag coefficient which is mainly a function of the bubble shape, A is the cross-sectional area of the bubble, and \dot{m}'' is the mass flux. The LiBr solution density varies from 1450 to 1650 kg/m^3 in our tests. Eq. (10) implies that a bubble experience a similar drag forces in LiBr solution and water flows as long as the LiBr solution flux is approximately 1.2–1.3 times higher than the water flux.

Overall, the results suggest that the bubbles could be fully vented from the flow as long as they stay in contact with the membrane. To do so, the bubbles should experience a sufficient residence time within the channels. Obviously, the residence time is

short for bubbles generated at the end of channels. Perhaps, the addition of a short adiabatic section at the desorber exit could resolve this issue.

Finally, it is noteworthy that the existing boiling literature provides significant insights on dynamics of flow boiling and bubble growth in microchannels. Notably, Kandlikar (2010) provides fundamental perspectives on scale effects on characteristics of the flow boiling process in microchannels. The existing knowledge on the flow boiling process and the insight provided here on characteristics of the membrane-based flow boiling desorption process may be utilized to analyze the impact of microchannels geometrical parameters on dynamics of the LiBr flow boiling and bubble growth.

6. Conclusions

A parametric study was conducted to understand characteristics of the water desorption process from a thin LiBr solution flow constrained by a porous hydrophobic membrane. The membrane mechanically constrained the solution flow while allowing the water vapor to exit the solution. Two modes of desorption consisting of: (1) direct diffusion of water molecules out of the solution film and their subsequent flow through the membrane and (2) formation of water vapor bubbles within the solution flow and their exit through the membrane were observed and analyzed. The vapor pressure determined the onset of direct diffusion desorption while the solution pressure determined the onset of the boiling desorption mechanism. The desorption rate increased moderately with temperature in the direct desorption mode and exponentially in the boiling desorption mode. Lowering the vapor pressure or elevating the water pressure inside the solution enhanced desorption through the direct diffusion mechanism, while the effect of solution velocity was negligible on the same. In the boiling desorption mode, increasing the solution pressure and velocity enhanced desorption at a fixed wall superheat temperature.

Comparison of the vapor mass flow rate through the membrane and the solution exit line showed that the ratio of the two is independent of the desorption rate implying that the membrane mass transfer resistance did not limit desorption through the membrane. However, the solution flow velocity directly affected the rate of bubble exit through the solution line. The bubbles exit rate was near zero at 0.75 kg/h flow rate and increased to a maximum of 20% of the total vapor generation at 3.25 kg/m² s mass flux. Visualization studies suggested that beyond a critical mass flux (i.e. flow velocity) some bubbles cease to extract through the membrane. To avoid this phenomenon, a membrane-based desorber can be designed to a width and length, for a given solution flow condition, to avoid the critical mass flux. Below the critical condition, adding an adiabatic section at the end of the microchannels is expected to enable full bubble extraction, as this approach increases the residence time of bubbles generated towards the end of the heated section.

The successful demonstration of a membrane-based desorption process in the set of tests presented in this study suggests that compact membrane-based desorber heat exchangers in a plate and frame configuration could be developed. This heat exchanger configuration is inherently more compact than the shell-and-tube heat exchangers and lends itself to small-scale, low capacity ARS designs. As opposed to a conventional shell-and-tube desorber, in this configuration, the liquid film thickness, velocity, and heating length can be controlled/optimized to maximize the desorber performance.

Acknowledgments

This study was funded by a grant from the Advanced Research Projects Agency – Energy (ARPA-E) under Contract DE-AR0000133.

References

- Abuaf, N., Black, S.H., Staub, F.W., 1985. Pool boiling performance of finned surfaces in R-113. *Int. J. Heat Fluid Flow* 6 (1), 23–30.
- Ali, A.H.H., 2010. Design of a compact absorber with a hydrophobic membrane contactor at the liquid–vapor interface for lithium bromide–water absorption chillers. *Appl. Energy* 87, 1112–1121.
- Ali, A.H.H., Shwerdt, P., 2009. Characteristics of the membrane utilized in a compact absorber for lithium bromide–water absorption chillers. *Int. J. Refrig.* 32, 1886–1896.
- Charters, W.W.S., Megler, V.R., Chen, W.D., Wang, Y.F., 1982. Atmospheric and sub-atmospheric boiling of H₂O and LiBr–H₂O solutions. *Int. J. Refrig.* 5 (2), 107–114.
- David, M.P., Steinbrenner, J., Miler, J., Goodson, K.E., 2009. Visualization and analysis of venting from a single microchannel two-phase copper heat exchanger. *ASME Conf. Proc.* 43604, 437–444.
- David, M.P., Steinbrenner, J.E., Miler, J., Goodson, K.E., 2011. Adiabatic and diabatic two-phase venting flow in a microchannel. *Int. J. Multiphase Flow* 37 (9), 1135–1146.
- Determan, M.D., Garimella, S., 2011. Ammonia–water desorption heat and mass transfer in microchannel devices. *Int. J. Refrig.* 34 (5), 1197–1208.
- Fujita, T., 1993. Falling liquid films in absorption machines. *Int. J. Refrig.* 16, 282–294.
- Garimella, S., Determan, M.D., Meacham, J.M., Lee, S., Ernst, T.C., 2011. Microchannel component technology for system-wide application in ammonia/water absorption heat pumps. *Int. J. Refrig.* 34 (5), 1184–1196.
- Hasaba, S., Uemura, T., Narita, H., 1961. *Refrigeration* 36, 622 (in Japanese).
- Herbine, G.S., Perez-Blanco, H., 1995. Model of an ammonia–water bubble absorber. *ASHRAE Trans.* 101, 1324–1332.
- Herold, E., Radermacher, R., Klein, S.A., 1996. *Absorption Chillers and Heat Pumps*. CRC Press, Boca Raton, FL.
- Hibiki, T., Ishii, M., 2003. Active nucleation site density in boiling systems. *Int. J. Heat Mass Transfer* 46 (14), 2587–2601.
- Hu, X., Lin, G., Cai, Y., Wen, D., 2011. Experimental study of flow boiling of FC-72 in parallel minichannels under sub-atmospheric pressure. *Appl. Therm. Eng.* 31 (17–18), 3839–3853.
- Islam, M.R., Wijesundera, N.E., Ho, J.C., 2003. Performance study of a falling-film absorber with a film-inverting configuration. *Int. J. Refrig.* 26, 909–917.
- Jani, S., Saidi, M.H., Mozafari, A., Heydari, A., 2004. Modeling of heat and mass transfer in falling film absorption generators. *Sci. Iran.* 11, 81–91.
- Johnson, M., Liddiard, G., Eddings, M., Gale, B., 2009. Bubble inclusion and removal using PDMS membrane-based gas permeation for applications in pumping, valving and mixing in microfluidic devices. *J. Micromech. Microeng.* 19 (9), 95011.
- Kamitani, A., Morishita, S., Kotaki, H., Arscott, S., 2009. Improved fuel use efficiency in microchannel direct methanol fuel cells using a hydrophilic macroporous layer. *J. Power Sources* 187 (1), 148–155.
- Kang, Y.T., Akisawa, A., Kashiwagi, T., 2000. Analytical investigation of two different absorption modes: falling film and bubble types. *Int. J. Refrig.* 23, 430–443.
- Kandlikar, S.G., 2010. Scale effects on flow boiling heat transfer in microchannels: a fundamental perspective. *Int. J. Thermal Sci.* 49, 1073–1085.
- Kim, D., Kim, M., 1999. Heat transfer enhancement characteristics for falling-film evaporation on horizontal enhanced tubes with aqueous LiBr solution. *J. Enhanced Heat Transfer* 6, 61–69.
- Kocamustafaogullari, G., Ishii, M., 1983. Interfacial area and nucleation site density in boiling systems. *Int. J. Heat Mass Transfer* 26 (9), 1377–1387.
- Lee, C.C., Chuah, Y.K., Lu, D.C., Chao, H.Y., 1991. Experimental investigation of pool boiling of lithium bromide solution on a vertical tube under subatmospheric pressures. *Int. Commun. Heat Mass Transfer* 18, 309–320.
- Lochovsky, C., Yasotharan, S., Günther, A., 2012. Bubbles no more: in-plane trapping and removal of bubbles in microfluidic devices. *Lab Chip* 12 (3), 595–601.
- Lonsdale, H.K., Merten, U., Riley, R.L., 1965. Transport properties of cellulose acetate osmotic membranes. *J. Appl. Polym. Sci.* 9, 1344–1362.
- Mason, E.A., Malinauskas, A.P., 1983. *Gas Transport in Porous Media: the Dusty-gas Model*. Elsevier, New York.
- Matsuda, A., Hada, K., Kawamura, T., 1990a. A vertical falling film type of absorber and generator for lithium bromide aqueous solutions. *Trans. Jpn. Assoc. Refrig.* 7, 47–56.
- Matsuda, A., Kawamura, T., Hada, K., 1990b. Evaporation for lithium bromide aqueous solution in a vertical falling film type of generator under reduced pressure. *Trans. Jpn. Assoc. Refrig.* 7, 35–45.
- Meng, D.D., Kim, J., Kim, C.-J., 2006. A degassing plate with hydrophobic bubble capture and distributed venting for microfluidic devices. *J. Micromech. Microeng.* 16 (2), 419–424.
- Nakoryakov, V.Y., Grigoriyeva, N.I., Lezhnina, S.I., Potaturkina, L.V., 1998. Combined heat and mass transfer in film absorption and bubble desorption. *Heat Trans. Res.* 29, 333–338.
- Nasr Isfahani, R., Moghaddam, S., 2013. Absorption characteristics of lithium bromide (LiBr) solution constrained by superhydrophobic nanofibrous structures. *Int. J. Heat Mass Transfer* 63, 82–90.
- Nishikawa, K., Fujita, Y., Ohta, H., Hidaka, S., 1982. Effects of system pressure and surface roughness on nucleate boiling heat transfer. *Memoirs of the Faculty of Engineering, Kyushu University* 42 (2), 95–111.
- Palacios, E., Izquierdo, M., Marcos, J.D., Lizarte, R., 2009. Evaluation of mass absorption in LiBr flat-fan sheets. *Appl. Energy* 86, 2574–2582.

- Qin, D., Xia, Y., Whitesides, G.M., 2010. Soft lithography for micro-and nanoscale patterning. *Nat. Protoc.* 5 (3), 491–502.
- Rainey, K.N., You, S.M., Lee, S., 2003. Effect of pressure, subcooling, and dissolved gas on pool boiling heat transfer from microporous, square pin-finned surfaces in FC-72. *Int. J. Heat Mass Transfer* 46, 23–35.
- Shi, C., Qinghua, C., Tien-Chien, J., Wang, Y., 2010. Heat transfer performance of lithium bromide solution in falling film generator. *Int. J. Heat Mass Transfer* 53, 3372–3376.
- Thorud, J.D., Liburdy, J.A., Pence, D.V., 2006. Microchannel membrane separation applied to confined thin film desorption. *Exp. Therm. Fluid Sci.* 30, 713–723.
- US Department of Energy, 2012. Annual Energy Review 2011. Document No. DOE/EIA-0384, Energy Information Administration, Washington, DC.
- Varma, H.K., Mehrotra, R.K., Agrawal, K.N., 1994. Heat transfer during pool boiling of LiBr–water solutions at subatmospheric pressures. *Int. Commun. Heat Mass Transfer* 21 (4), 539–548.
- Velders, G.J., Fahey, D.W., Daniel, J.S., McFarland, M., Andersen, S.O., 2009. The large contribution of projected HFC emissions to future climate forcing. *Proc. Natl. Acad. Sci.* 106 (27), 10949–10954.
- Wijmans, J.G., Baker, R.W., 1995. The solution-diffusion model: a review. *J. Membr. Sci.* 107 (1), 1–21.
- Xu, J., Vaillant, R., Attinger, D., 2010. Use of a porous membrane for gas bubble removal in microfluidic channels: physical mechanisms and design criteria. *Microfluid. Nanofluid.* 9 (4), 765–772.
- Yoon, J.I., Kwon, O.K., Bansal, P.K., Moon, C.G., Lee, H.S., 2006. Heat and mass transfer characteristics of a small helical absorber. *Appl. Therm. Eng.* 26 (2–3), 186–192.
- Yoon, J.-I., Phan, T.-T., Moon, C.-G., Bansal, P., 2005. Numerical study on heat and mass transfer characteristic of plate absorber. *Appl. Therm. Eng.* 25, 2219–2235.
- Yoshitomi, H., Tajima, O., Takeuchi, T., Hara, H., 1981. *Refrigeration* 56, 271 (in Japanese).
- Yu, D., Chung, J., Moghaddam, S., 2012. Parametric study of water vapor absorption into a constrained thin film of lithium bromide solution. *Int. J. Heat Mass Transfer* 55, 5687–5695.
- Zhu, X., 2009. Micro/nanoporous membrane based gas–water separation in microchannel. *Microsyst. Technol.* 15 (9), 1459–1465.